Estimating the metallicity of star-forming early-type galaxies

Yu-Zhong Wu ⬛⋆ and Wei Zhang

CAS Key Laboratory of Optical Astronomy, National Astronomical Observatories, Beijing, 100101, China

ABSTRACT

We derive data for 4615 star-forming early-type galaxies (ETGs), which come from a cross-match of the Galaxy Zoo and the catalogue of the Max Planck Institute for Astrophysics–Johns Hopkins University (MPA–JHU) emission-line measurements for the Sloan Digital Sky Survey Data Release 7. Our sample is distributed mainly at $-0.7 < \log(\mathrm{SFR}/(\mathrm{M}_{\odot}\,\mathrm{yr}^{-1})) < 1.2$, and the median value of our star formation rates (SFRs) is slightly higher than that shown in Davis & Young. We show that there is a significant trend of lower/higher stellar mass ETGs having lower/higher SFRs, and we obtain our sample best fit of $\log(\mathrm{SFR}/(\mathrm{M}_{\odot}\mathrm{yr}^{-1})) = (0.74 \pm 0.01)\log(\mathrm{M}_*/\mathrm{M}_{\odot}) - (7.64 \pm 0.10)$. We find the same slope as found by Cano-Díaz et al. In our star-forming ETG sample, we demonstrate clearly the correlation of the stellar mass–metallicity (MZ) relation. We find that higher metallicity measurements may be introduced by the diffuse ionized gas, when the D16, Sanch18 and Sander18 indicators are used to calibrate the metallicity of ETGs. We show the relations between the SFR and $12 + \log(\mathrm{O/H})$ with different metallicity estimators, and we suggest that their correlations may be a consequence of the SFR–stellar mass and MZ relations in ETGs.

Key words: galaxies: abundances – galaxies: elliptical and lenticular, cD – galaxies: evolution.

1 INTRODUCTION

Some galaxy surveys reveal the two different locales in the colour–stellar magnitude diagram: the 'red cloud' and the 'blue cloud' (Baldry et al. 2004). The blue cloud contains blue, star-forming late-type galaxies (disc-dominated), while the red cloud includes red, passive early-type galaxies (ETGs; elliptical, S0 and bulge-dominated spiral). In optical colour–magnitude/mass diagrams, the red cloud generally denotes ETGs. Based on a visual classification of images of Sloan Digital Sky Survey (SDSS) galaxies, ETGs contain morphologically elliptical and lenticular galaxies, and it is suggested that these galaxies are 'red and dead' objects.

Ultraviolet (UV) observations confirm recent star formation in many ETGs, and the *Galaxy Evolution Explorer* (*GALEX*) and the *Hubble Space Telescope* (*HST*) provide a good way to trace the detection of star formation in ETGs. Using the *GALEX* photometric data, Yi et al. (2005) have shown that the near-UV colour–magnitude relation is a perfect instrument, tracing the late star formation history, and that it demonstrates signs of recent star formation in ETGs. Combining the SDSS data release 3 (DR3) and *GALEX* Medium Imaging Survey, Kaviraj et al. (2007) found some recent star formation in ≥ 30 per cent of the ETG sample of 2100 galaxies during $\lesssim 1$ Gyr. Studying NGC 4150 near-UV/optical data from the Wide Field Camera 3 on the *HST*, Crockett et al. (2011) exhibited recent star formation, fuelled by a large reservoir of molecular gas induced by a minor merger, and suggested that $\sim$ 2–3 per cent of the stellar mass is contributed by the star formation.

The gas that fuels low-level star formation has various sources, and it can be classified into internal and external processes. The internal mechanism contains stellar mass loss, while the external process includes mainly accretion of cold gas, hot gas and clumpy accretion (Bryant et al. 2019). Using the CO detections of ETGs in single-dish surveys, Young (2005) suggested that stellar mass loss could have resulted in the molecular gas in some ETGs, and also found some evidence that the molecular gas is traced from both internal and external processes in NGC 83 and 2320. Using the GALFORM model of galaxy formation, Lagos et al. (2014) found that radiative cooling from the hot haloes of ETGs provides neutral gas content in a majority of ETGs at $z \approx 0$. Obtaining H I synthesis imaging data of three ETGs, Chung et al. (2012) investigated their gas environment and H I properties, and found some H I gas directly from neighbours, which is evidence for cold gas accretion. Considering gas inflows in various mergers or interactions between galaxies, clumpy accretion is also an external process.

Late-type galaxies can quench star formation if they lack enough supply of various gases, and their sites will change from the blue cloud to the red cloud on the colour–magnitude diagram (e.g. Faber et al. 2007; Cortese & Hughes 2009). At the same time, much evidence shows that the stellar mass in red cloud galaxies has been increasing (e.g. Bell et al. 2004; Brown et al. 2007). As a result of various major mergers, minor mergers and the inflow of the intergalactic medium, ETGs can accrete various gases, triggering star formation, which will then drive the ETGs to migrate from the red cloud to the blue cloud on the colour–magnitude diagram.

Schawinski et al. (2009) used the SDSS DR6 and $u–r$ colour data to obtain 204 star-forming blue ETGs with the help of the visual morphology from the Galaxy Zoo. These ETGs have significantly more blue $u–r$ colour than the red cloud galaxies with higher SFRs $(0.5 < \mathrm{SFR}/(\mathrm{M}_{\odot}\ \mathrm{yr}^{-1}) < 50)$, and their sample provides SFRs and emission-line classification. Utilizing the SDSS DR7 and Galaxy Zoo 1, Davis & Young (2019) derived a larger sample of star-forming elliptical galaxies – based on the standard of Kauffmann et al. (2003a), on the Baldwin–Phillips–Terlevich (BPT) diagram

⋆ E-mail: yzwu@nao.cas.cn

(Baldwin, Phillips & Terlevich [1981]) – with the metallicity measurements. The median value is 2 $M_\odot$ yr^{-1} in their ETG sample.

Several works claim to explore the properties of ETGs, and they demonstrate that these ETGs have significant SFR measurements. In this study, we mainly focused on the SDSS DR7 and Galaxy Zoo 1 to derive the star-forming ETG sample. We also study the distributions of various parameters and compare them with star-forming galaxies (SFGs) or composite ETGs. (These galaxies are defined as the ETG sample, which lies in the composite region on the BPT diagram, and these ETGs are called composite ETGs in this paper.) In addition, we estimate their metallicities with six abundance indicators. In Section 2, we describe the ETG sample and data in detail. We present sample properties of our star-forming ETGs in Section 3. In Section 4, we calibrate their metallicities with six abundance estimators, and describe the metallicity properties of our ETG sample. A summary of our results is shown in Section 5.

2 THE DATA

In this study, our sample is chosen from the data of the SDSS Data Release 7 (DR7; Abazajian et al. [2009]). In the SDSS DR7 catalogue of Max Planck Institute for Astrophysics−John Hopkins University (MPA–JHU), we can utilize measurements of emission-line fluxes, stellar masses, redshifts and SFRs of about 900 000 galaxies, and these are publicly available.

In this work, we study star-forming ETGs, and we adopt a similar method to that of Wu ([2020]) to select our sample, before the BPT diagram is used to choose the composite ETG sample. Based on a wavelength range of 3800–9200 Å of the SDSS spectra, we select the lower limit ($z \approx 0.023$) of redshifts in our sample, and we can be assured that [O II] $\lambda\lambda 3227, 3229$ will appear in the observed range (Wu & Zhang [2013]). The upper limit of redshift is 0.2 in our study. We need to restrict the aperture-covering fraction to > 20 per cent, and the fraction is computed from the fibre and Petrosian magnitudes in the *r* band. We select these galaxies, which have a signal-to-noise ratio (S/N) > 3 for Hα and S/N > 2 for [O II] $\lambda\lambda 3227, 3229$, and [N II] $\lambda 6584$. Regarding the SFR measurement in the catalogue, we require an SFR FLAG keyword, describing the status of the SFR measurements, to be equal to zero. In consequence, 231 666 galaxies constitute our initial sample.

For the ETG selection, we take the two judgement standards to select our ETGs (Wu [2020]). One criteria is that the galaxies should satisfy $n_{Sersic} > 2.5$, and the other is that the elliptical probability is larger than 0.5 (Herpich et al. [2018]), which comes from Galaxy Zoo 1 (Lintott et al. [2008], [2011]). The measurement of the Sérsic index is chosen from the New York University Value-Added Galaxy Catalog (NYU-VAGC; Blanton et al. [2005]). First, we cross-match the NYU-VAGC with our initial sample within 2 arcsec, and we choose galaxies with $n_{Sersic} > 2.5$. Then we use the elliptical probability of >0.5 to select ETGs (Herpich et al. [2018]), and match these $n_{Sersic} > 2.5$ galaxies with those found in table 2 of Lintott et al. ([2011]) within 2 arcsec. Finally, we derive an ETG sample of 28 093 objects.

In this paper, we study these ETGs, which come from the above-mentioned ETG sample and also lie in the H II region on the BPT diagram: they are called star-forming ETGs. The topic of ionized gas has been discussed in many recent articles, and in particular in the two recent reviews on the topic by Sánchez ([2020], figs 1 and 5, and main text) and Sánchez et al. ([2020], figs 2–6, section 4). To obtain a reliable ETG sample, we cannot define definitive boundaries only using the BPT diagram, and other additional parameters are required.

The ionization can be studied and discussed through the global and local dominance (Stasińska et al. [2008]; Cid Fernandes et al. [2010]; Sánchez et al. [2014]; Lacerda et al. [2018], [2020]). In general, if the EW(Hα) < 6 Å (for the SDSS aperture), it is difficult to justify that the observed ionization is due to star formation (Stasińska et al. [2008]; Cid Fernandes et al. [2010]). Also, the velocity dispersion may be a better classification of the ionization (not for the SDSS single fibre; D'Agostino et al. [2019]). Finally, other line ratios should be considered, as the use of the BPT diagram in addtion to the EW(Hα) is not enough to exclude other ionizing sources, such as low-metallicity weak AGNs and shocks. Shock ionization is nowadays known to be present in ETGs (Cheung et al. [2016]; Dopita et al. [2016]; López-Cabá et al. [2020]). Its EW(Hα) can take any value, and can be observed in any location in the BPT diagram. Moreover, the use of other line ratios, such as [S II]/Hα and [O I]/Hα, can improve the classification of the ionization (Kewley et al. [2001]; Sánchez [2020]). We select our sample ionized by star formation by adopting three conditions: (i) the Kauffmann et al. ([2003a]) line for the BPT diagram; (ii) the Kewley et al. ([2001]) demarcation lines in [S II]/Hα versus [O III]/Hβ and [O I]/Hα versus [O III]/Hβ; (iii) the Hα equivalent width EW(Hα) > 6 Å (Cid Fernandes et al. [2010]). As these galaxies are dominated by star formation activity, we consider contribution of star formation on photoionization from these galaxies. Here, we obtain 4615 star-forming ETGs.

In the measurements of M_* (Kauffmann et al. [2003b]) and SFR (Brinchmann et al. [2004]), we adopt the total stellar mass and total SFR from the MPA–JHU catalogue. The mass-to-light ratios and the *z*-band attenuation values within the SDSS fibre are extrapolated to the whole galaxy, under the assumption that the fibre emission-line contribution is the same as the global one. The total mass is calculated by multiplying the dust-corrected and K-corrected luminosity of the galaxy by the mass-to-light ratio estimate. The SFR is derived using the Hα flux within the SDSS fibres, and fibre- correction using the galaxy colours is purely empirical. All aperture bias in SFR estimates can be corrected in a statistical way (Brinchmann et al. [2004]). In addition, we need to correct a Chabrier ([2003]) initial mass function (IMF) from a Kroupa ([2001]) IMF assumed in the MPA–JHU catalogue for the SDSS DR7. Because our ETG sample is selected by using the above-mentioned three conditions, we can use various metallicity calibrators to estimate the gas-phase oxygen abundance. The O3N2 index introduced by Alloin et al. ([1979]) depends on [O III]/Hβ and [N II]/Hα. One of the most popular calibrations relates the index and the metallicity using $12 + \log(O/H) = 8.73 - 0.32 \times O3N2$ proposed by Pettini & Pagel ([2004]). There have been several updates of this calibrator (Nagao, Maiolino & Marconi [2006]; Pérez-Montero & Contini [2009]). The calibrator has been recently updated by Marino et al. ([2013]), and we adopt the calibrator in this study. Also, we use the following various metallicity calibrators: D16, the N2S2Hα method of Dopita et al. ([2016]); Jon15, the O32 method of Jones, Martin & Cooper ([2015]); Curti17, the O3S2 method of Curti et al. ([2017]); Sanch18, the N2 method of Sánchez-Almeida et al. ([2018]); Sander18, the N2O2 method of Sanders et al. ([2018]).

3 SAMPLE PROPERTIES OF STAR-FORMING EARLY-TYPE GALAXIES

In this section, we describe the various properties of the star-forming ETG sample. In Fig. [1], we show these star-forming ETGs on the BPT diagram. The Kauffmann et al. ([2003a]) semi-empirical lower boundary for SFGs is shown by the blue dot-dashed curve. Our sample of star-forming ETGs is displayed by the black dots. We can
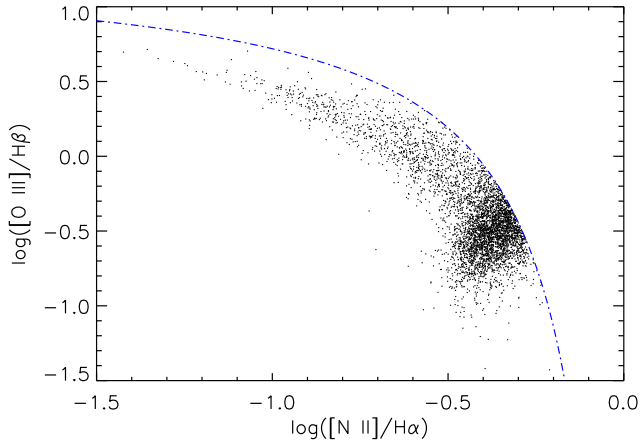
Figure 1. Traditional diagnostic diagram. The black dots are star-forming ETGs. The blue dot-dashed line shows the semi-empirical lower limit of Kauffmann et al. (2003a) for SFGs.
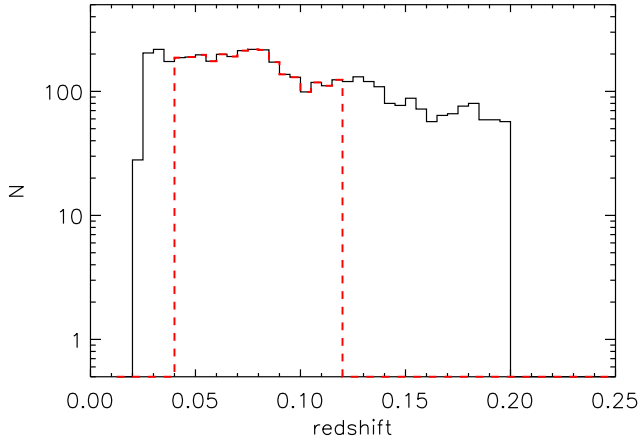

Figure 2. Distributions of redshift for star-forming ETGs. The black solid and red dashed lines display the samples of star-forming ETGs with $0.023 < z < 0.2$ and $0.04 < z < 0.12$, respectively.

see that most of our star-forming ETGs are located in a small region on the BPT diagram.

In Fig. 2, the redshift distributions of our star-forming ETG sample are shown. The red dashed and black lines represent the distributions of ETGs with $0.04 < z < 0.12$ and $0.023 < z < 0.2$, respectively. The former sample size accounts for ~ 58 per cent of the latter. We can see that the sample size does not change clearly from redshift $z = 0.025$ to $z = 0.07$, and that the size generally decreases with increasing redshift at $z \gtrsim 0.08$. This shows that the size of our ETG sample is significantly affected by redshift, and indicates that the star-forming ETG sample with $0.023 < z < 0.2$ can be used to study various properties of ETGs.

Fig. 3(a) describes the distributions of stellar mass for the star-forming ETG samples. The black solid and red dashed lines represent the distributions of star-forming ETGs with $0.023 < z < 0.2$ and $0.04 < z < 0.12$, respectively. Compared with the distribution (occupying mainly the lower stellar mass part of the ETGs with $0.023 < z < 0.2$) of stellar mass for composite ETGs (Wu 2021), the $0.04 < z < 0.12$ star-forming ETGs take up the centre region of the distribution of stellar mass for star-forming ETGs with $0.023 < z < 0.2$. In the $0.04 < z < 0.12$ star-forming ETG sample, it distributes mainly at $9.5 < \log(M_*/M_\odot) < 11.0$, accounting for 91 per cent

of the ETG sample. The star-forming ETGs with $0.023 < z < 0.2$ distribute mainly at $9.0 < \log(M_*/M_\odot) < 11.5$, occupying 97 per cent of our ETG sample. This indicates that star-forming ETGs will have different main distribution ranges of stellar mass when we select ETG samples with different redshift ranges. We find that both star-forming ETG samples have a broader range of distribution for stellar mass. The ETG sample with $0.04 < z < 0.12$ has a median value of $\log(M_*/M_\odot) = 10.36$, and the star-forming ETGs with $0.023 < z < 0.2$ present a median value of $\log(M_*/M_\odot) = 10.50$. Compared with the median value, $\log(M_*/M_\odot) = 10.75$, of stellar masses in composite ETGs (Wu 2021), the median value of star-forming ETGs decreases by ~ 0.25 dex.

In Fig. 3(b), we show the distribution of SFR for star-forming ETG samples. The distributions of SFR for $0.023 < z < 0.2$ and $0.04 < z < 0.12$ star-forming ETGs are displayed by the black solid and red dashed lines, respectively. The distribution of star-forming ETGs with $0.04 < z < 0.12$ occupies the lower SFR section of the ETGs with $0.023 < z < 0.2$. In the $0.04 < z < 0.12$ star-forming ETG sample, $-0.5 < \log(SFR/(M_\odot yr^{-1})) < 1.0$ is the main distribution of SFR, accounting for 91 per cent of the ETG sample. The $0.023 < z < 0.2$ star-forming ETG sample distributes mainly at $-0.7 < \log(SFR/(M_\odot yr^{-1})) < 1.2$, taking up 91 per cent of our ETG sample. The median values of the former and latter ETG samples are 2.3 $M_\odot$ yr^{-1} and 3.1 $M_\odot$ yr^{-1}, respectively. Compared with the median value (2 $M_\odot$ yr^{-1}) of SFRs of Davis & Young (2019), our star-forming ETG sample has a slightly higher median value of SFRs than that in Davis & Young (2019).

In Fig. 4, we show the distribution of stellar mass and SFR (M–SFR) for star-forming ETGs. Overall, the distributions of our ETG and the SDSS SFG samples are similar, and most of our star-forming ETGs lie on the 'main sequence' (Noeske et al. 2007; Cano-Díaz et al. 2019). The best fit of the MaNGA data at $z \sim 0$ from Cano-Díaz et al. (2019) assumed a Salpeter IMF (Salpeter 1955) is exhibited by the red dot-dashed line, and the green solid line represents the best least-squares fit for our star-forming ETGs. We obtain the fit of $\log(SFR/(M_\odot yr^{-1})) = (0.74 \pm 0.01)\log(M_*/M_\odot) - (7.22 \pm 0.08)$, and our data have the same slope as the SFGs found in Cano-Díaz et al. (2019), showing a slope of 0.74 ± 0.01. Also, our fit lies above the main sequence from Cano-Díaz et al. (2019), slightly higher by $\sim 0.3-0.4$ dex. Because the stellar mass/SFR provided by a Salpeter IMF is higher by ~ 0.25 dex than that by a Chabrier IMF (Panter et al. 2007; Dutton et al. 2011), the offset is mainly due to some IMF selection effect. The galaxy stellar mass and SFR are correlated with each other, and the close correlation is designated as the main sequence of SFGs (Noeske et al. 2007). A significant tendency for lower/higher stellar mass ETGs to have lower/higher SFR is shown. Compared with the correlation (the Spearman coefficient $r = 0.60$) of composite ETGs (Wu 2021), we have the better correlation, showing the Spearman coefficient $r = 0.82$. This indicates that these star-forming ETGs still obey the fundamental relation of SFGs, although they actually belong to the ETGs. In this paper, the stellar mass and SFR are derived by using the fibre corrections. If the covering fraction of a galaxy is >0.20, the systematic and random errors induced by the aperture effect would be minimized (Kewley, Jansen & Geller 2005). The median value of the covering fraction of our sample is 0.38, and so our result may be rarely influenced by the aperture effect.

In Table 1, the different parameters of the star-forming ETG sample are demonstrated. From the MPA–JHU catalogue, we present RA, Dec., stellar masses, redshifts, SFRs, and the fibre and petro flux ratio (frac). We also provide the metallicity measurements with six abundance indicators for our star-forming ETGs.
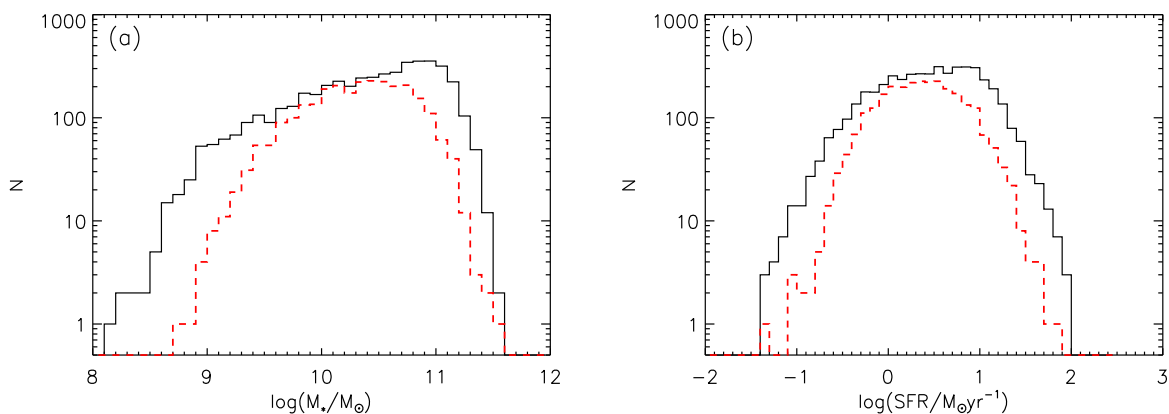
Figure 3. Comparison of stellar mass (left-hand panel) and SFR (right-hand pane) distributions for star-forming ETGs with different redshift ranges. The black and red dashed lines are the same as in Fig. 2.
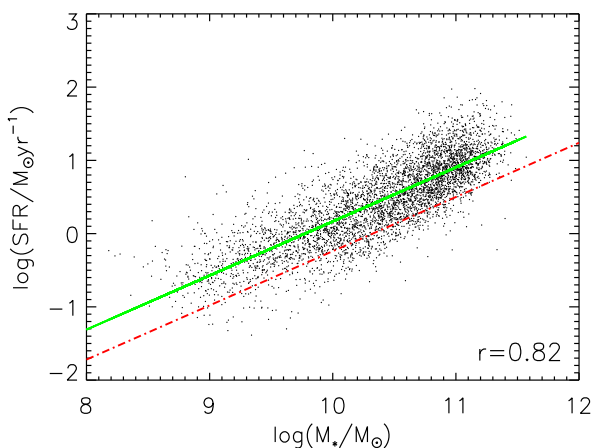

Figure 4. The SFR–M relation for star-forming ETGs. The red dot-dashed and green lines represent the best fits of Cano-Díaz et al. (2019) and this study for their corresponding data, respectively.

4 METALLICITY PROPERTIES OF STAR-FORMING EARLY-TYPE GALAXIES

Because the star-forming ETGs are selected by using the above-mentioned three conditions, we can use various metallicity indicators applied for SFGs to calculate the metallicity of these ETGs based on photoionization models and some empirical methods. In Fig. 5, we use the six metallicity indicators to present the mass–metallicity (MZ) relation for our star-forming ETGs. Compared with the stellar mass range of $10.0 < \log(M_*/M_\odot) < 11.0$ of most composite ETGs in Wu (2020), the range of most galaxy stellar masses of our star-forming sample significantly increases, from $\log(M_*/M_\odot) \sim 9.0$ to ~ 11.3. Compared with the correlation of the MZ relation in composite ETGs (Wu 2020), these MZ relations of our star-forming ETGs show significantly the positive correlation. This may be due mainly to the fact that our ETG sample has a wider range of stellar mass.

Fig. 5 shows the MZ relations with colour bars of EW(Hα). The colour bar presents the EW(Hα) values per bin in the MZ relations. We can see that star-forming ETGs with higher EW(Hα) values tend to have stronger star formation, and they often present lower metallicity. This is consistent with the result of SFGs (e.g. Mannucci et al. 2010). In our study, the metallicity is obtained by using the SDSS spectra within an aperture of 3 arcsec. In Iglesias-

Páramo et al. (2016), the average difference between fibre-based and aperture-corrected metallicities, a typical value, is a maximum of 0.047 dex (11 per cent) for different redshift and stellar mass ranges. It depends on the calibrator adopted, and it is still within the typical uncertainties of metallicities calibrated by empirical estimation, though the average difference is systemically a bias. These results indicate that these ETGs almost follow the property of SFGs in the MZ relation, and present a good correlation.

In Fig. 5, all the green dashed lines correspond to the polynomial fits for 148 824 SFGs with $0.023 < z < 0.3$, obtained from the MPA–JHU catalogue for the SDSS DR7 by using the same method of sample selection of Wu, Zhang & Zhao (2019), except that the [O II] $\lambda\lambda 3227$, 3229, and [N II] $\lambda 6584$ have S/N >2. Each fit is based on median values of 30 bins, and there is 0.1 dex in mass, including more than 200 galaxies. The MZ relations for our star-forming ETGs are basically consistent with the fit of the above-mentioned large SFG sample. Figs 5(a)–(f) utilize the metallcity estimators of Ma13, Jon15, Curti17, D16, Sanch18 and Sanders18, respectively, to calibrate the metallicities of our star-forming ETG sample. The MZ relation of Fig. 5(a) presents a significant correlation, with the Spearman coefficient $r = 0.57$. Figs 5(c)–(f) also show the positive correlation, and their Spearman coefficients are $r = 0.61$, $r = 0.70$, $r = 0.55$ and $r = 0.67$, respectively. In Fig. 5, we show each metallicity dispersion, calculated in bins of 0.1 dex in M_*, for each metallicity calibrator. Fig. 5(b) does not exhibit clearly a positive correlation, with the Spearman coefficient $r = 0.29$. In addition, these correction coefficients can be used to compare the strength of correlations between stellar mass and metallicity, but we should consider that the MZ relations of Fig. 5 are sometime not monotonic.

In Wu (2020), because the two metallicity indicators of Sanch18 and Sander18 show metallicity increasing with N-enrichment, both indicators cannot calibrate the ETG metallicity. The cyan solid lines of Fig. 5 show a polynomial fit of star-forming ETGs. Each fit is based on median values of 27 bins, 0.1 dex in mass, and each bin contains no less than two ETGs. We can see that most star-forming ETGs locate around the green fitting line of SFGs in each figure. Compared with Figs 4(b) and (e) of Wu (2020), Figs 5(d)–(f) show that about 67 per cent, 68 per cent and 66 per cent of star-forming ETGs lie above the median MZ relation of large sample SFGs (148 824 SFGs). This may be attributed to the effect of [N II]/Hα ratios from the so-called diffuse ionized gas (DIG). In single-aperture spectra integrating a substantial fraction of a galaxy, such as the SDSS data, and in particular for ETGs, it is impossible to observe just

Table 1. Sample of the star-forming ETGs.

RA (J2000) (1)	Dec. (J2000) (2)	Redshift (3)	log(M_*) ($M_\odot$) (4)	log(SFR) ($M_\odot$ yr^{-1}) (5)	frac[a] (6)	12 + log(O/H) Ma13 (7)	Jon15 (8)	Curti17 (9)	D16 (10)	Sanch18 (11)	Sander18 (12)
11 39 37.2	21 18 05.4	0.16	10.95	1.43	0.38	8.59 ± 0.02	8.58 ± 0.04	8.81 ± 0.02	9.02 ± 0.03	8.80 ± 0.01	9.31 ± 0.03
13 43 02.6	18 52 21.0	0.08	10.46	0.41	0.44	8.58 ± 0.01	8.64 ± 0.03	8.76 ± 0.01	8.75 ± 0.02	8.78 ± 0.01	9.12 ± 0.02
13 54 58.1	60 30 54.0	0.09	10.40	−0.07	0.50	8.57 ± 0.02	8.63 ± 0.05	8.75 ± 0.02	8.83 ± 0.04	8.80 ± 0.02	8.96 ± 0.04
08 18 32.2	29 48 03.6	0.08	10.58	0.39	0.32	8.56 ± 0.02	8.61 ± 0.05	8.79 ± 0.02	8.90 ± 0.05	8.74 ± 0.01	9.10 ± 0.04
15 35 24.7	08 58 08.4	0.05	9.77	−0.15	0.42	8.54 ± 0.01	8.61 ± 0.02	8.74 ± 0.01	8.71 ± 0.01	8.74 ± 0.01	8.99 ± 0.02
08 01 38.4	19 34 49.8	0.12	10.91	0.87	0.31	8.59 ± 0.02	8.63 ± 0.06	8.83 ± 0.02	8.93 ± 0.04	8.74 ± 0.01	9.17 ± 0.03
13 58 18.7	06 25 53.3	0.18	10.85	1.51	0.39	8.47 ± 0.01	8.35 ± 0.03	8.67 ± 0.01	9.01 ± 0.04	8.75 ± 0.01	9.25 ± 0.03
15 08 04.1	04 04 49.2	0.09	10.82	1.27	0.44	8.53 ± 0.00	8.56 ± 0.01	8.73 ± 0.00	8.87 ± 0.01	8.79 ± 0.00	9.06 ± 0.01
15 05 01.7	08 20 12.4	0.09	10.16	−0.48	0.50	8.41 ± 0.01	8.53 ± 0.02	8.55 ± 0.02	8.44 ± 0.05	8.69 ± 0.02	8.56 ± 0.03
13 19 02.6	08 14 29.6	0.13	10.95	0.04	0.27	8.48 ± 0.03	8.59 ± 0.05	8.64 ± 0.03	8.63 ± 0.05	8.77 ± 0.03	8.89 ± 0.05
...	...	...	...	...	...	...	...	...	...	...	...

[a]Values were calculated from the fibre flux and petro flux ratio.
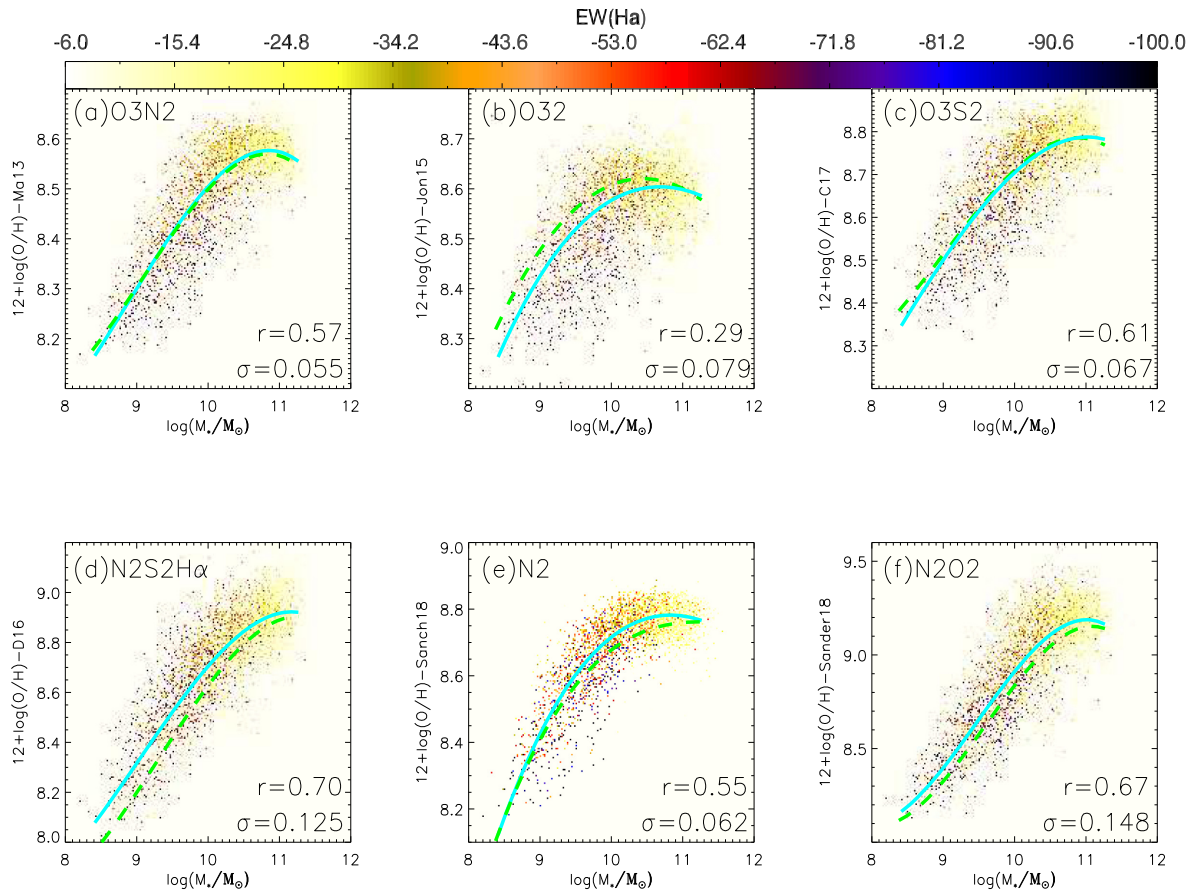
Figure 5. Comparison of the MZ relations of star-forming ETGs using the colour bar of EW(Hα), and their abundance estimators Ma13, Jon15, Culti17, D16, Sanch18, and Sander18, respectively. The green dashed and cyan solid lines show the polynomial fits of data from 148 824 SFGs (see Section 2) and star-forming ETGs, respectively.

single/pure ionization. In the case of ETGs, the effects of shocks and, in particular, diffuse ionization (from the DIG) due to hot evolved stars are ubiquitous in this type of galaxy (e.g. Singh et al. 2013; Sánchez et al. 2014; Belfiore et al. 2017). Although the EW(Ha) of those contaminations – similar to low-ionization nuclear emission-line regions (LINERs), in general – may be lower than that of the star formation regions, the [N II]/Hα ratio will increase significantly (Zhang et al. 2017). This means that the contamination by this source pushes the line ratios toward some larger values of [N II]/Hα. This

way, applying an oxygen abundance calibrator that uses the N2 ratio for an ionized gas with this kind of contamination produces an erroneous abundance. This is also true for any calibrator using [S II]. To provide a more reliable estimation of the abundance, it is necessary to decontaminate this component. However, this is in general difficult (e.g. Mast et al. 2014; Davies et al. 2016; Espinosa-Ponce et al. 2020), and for single-fibre spectroscopic data, it is nearly impossible, unless certain assumptions are made. This is attributed to the N2S2Hα, N2 and N2O2 indices from the D16, Sanch18 and

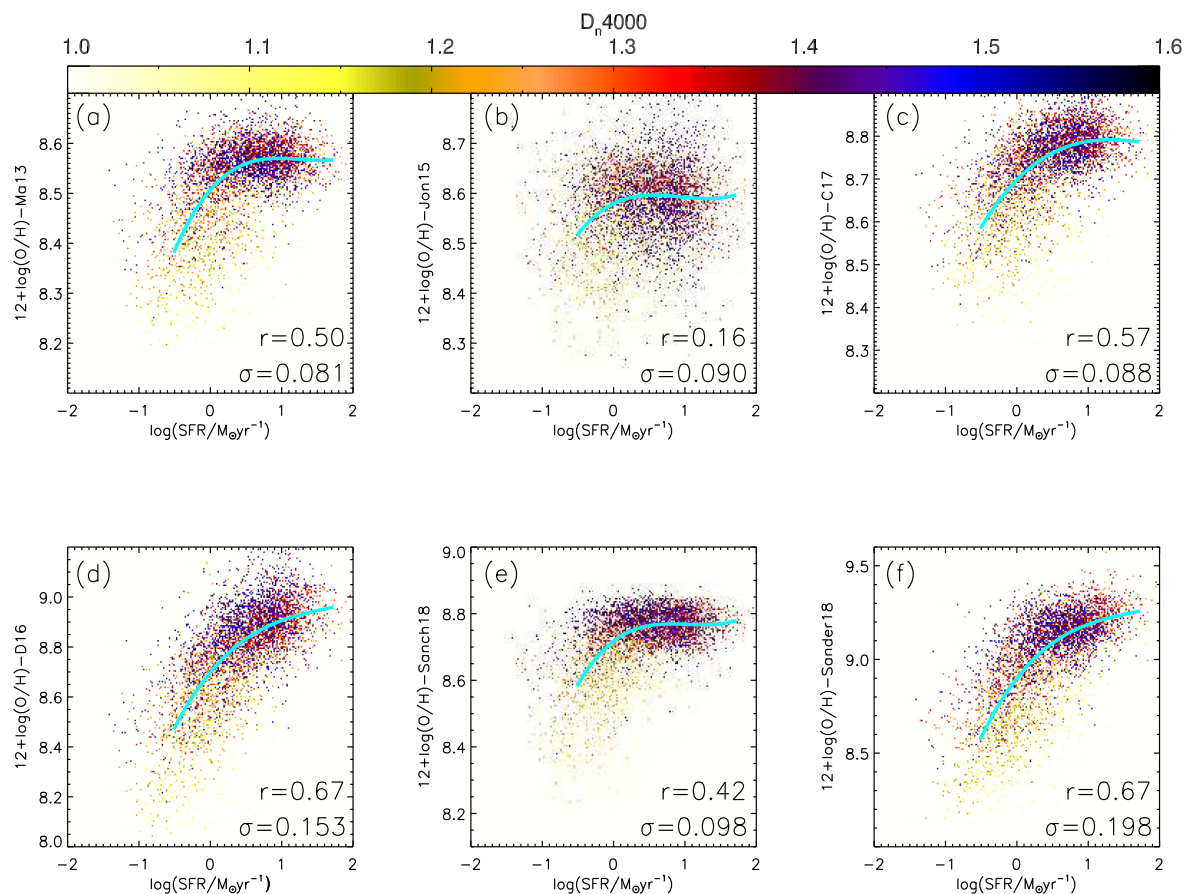**Figure 6.** Comparison of SFR–Z relations with the colour bar of D_n4000 for star-forming ETGs; these metallicity indicators are the same as in Fig. 5. The cyan solid lines represent the polynomial fits of star-forming ETGs.

Sander18 estimators, and we suggest that the three calibrators bring higher metallicity measurements. These results indicate that star-forming ETGs with low-level star formation are different from the general population of SFGs. Their ionization may be dominated by star formation, but they present a mix of other ionization sources, as they are at least partially retired.

In Fig. 6, we describe the distributions of SFR and metallicity calibrated by the six metallicity indicators. Fig. 6(a) uses the Ma13 estimator to present the relation between SFR and $12 + \log(O/H)$ (SFR–Z), showing significantly a positive correlation, and the Spearman coefficient is $r = 0.50$. In SFGs, we use the data of Wu et al. (2019) – that is, the metallicity calibrated by the O3N2 indicator of Pettini & Pagel 2004 (PP04) and the O3N2 indicator simultaneously utilized by the PP04 and Ma13 calibrators − to show the SFR–Z relation. We find that these data display a weak correlation, with a Spearman coefficient $r = 0.34$, and are consistent with the results found by Yates & Kauffmann (2014). In Fig. 6(b), the relation between SFR and $12 + \log(O/H)$ is shown, and it does not present a correlation, with the Spearman coefficient $r = 0.16$. This denotes that the correlation between SFR and metallicity may depend on the metallicity indicator.

In Figs 6(c)–(f), the metallicities are calibrated by the Curti17, D16, Sanch18 and Sander18 calibrators, respectively, and we display their distributions of SFR and metallicity. We can see that they present a significant correlation, and that their Spearman coefficients are $r = 0.57$, $r = 0.67$, $r = 0.55$ and $r = 0.67$, respectively. In Fig. 6, the cyan lines represent the polynomial fits of our ETGs.

Each fit is based on median values of 23 bins, 0.1 dex in log(SFR), and each bin includes more than 28 ETGs. Fig. 6 shows each metallicity dispersion, calculated in bins of 0.1 dex in log(SFR), for each metallicity calibrator. These results show that almost all the relations between SFR and $12 + \log(O/H)$ exhibit clearly a significant correlation, except the relation (calibrated by Jon15 indicator) in Fig. 6(b). Compared with the weak correlation between SFR and metallicity in the composite ETG sample (Wu 2021), the two parameters of our star-forming ETGs present a significant correlation. This indicates that our star-forming ETG sample has a better correlation in the SFR–Z relation than the SFG and composite ETG samples.

In Fig. 6, we also display the SFR–Z relations with colour bars of D_n4000. The colour bar presents the age distribution in the SFR–Z relations. From Fig. 6, star-forming ETGs with a higher D_n4000 index often show higher metallicity. On the whole, this is consistent with the result that SFGs that have a higher D_n4000 index demonstrate higher metallicities at a given stellar mass/SFR (Lian et al. 2015; Wu et al. 2019).

In addition to the differences between the bulk population of star-forming ETGs and SFGs, we further explore the differences between both types of galaxies. In Fig. 7, we use the colour bars of stellar mass to show the SFR–Z relations of star-forming ETGs and SFGs – the sample of 83 159 SFGs is obtained by using the method of Wu et al. (2019) and our three selection conditions for ensuring these SFGs are ionized by star formation – at $\log(M_*/M_\odot) < 10.0$ and $\log(M_*/M_\odot) > 10.0$, respectively. The metallicity of Fig. 7 is calibrated by the D16
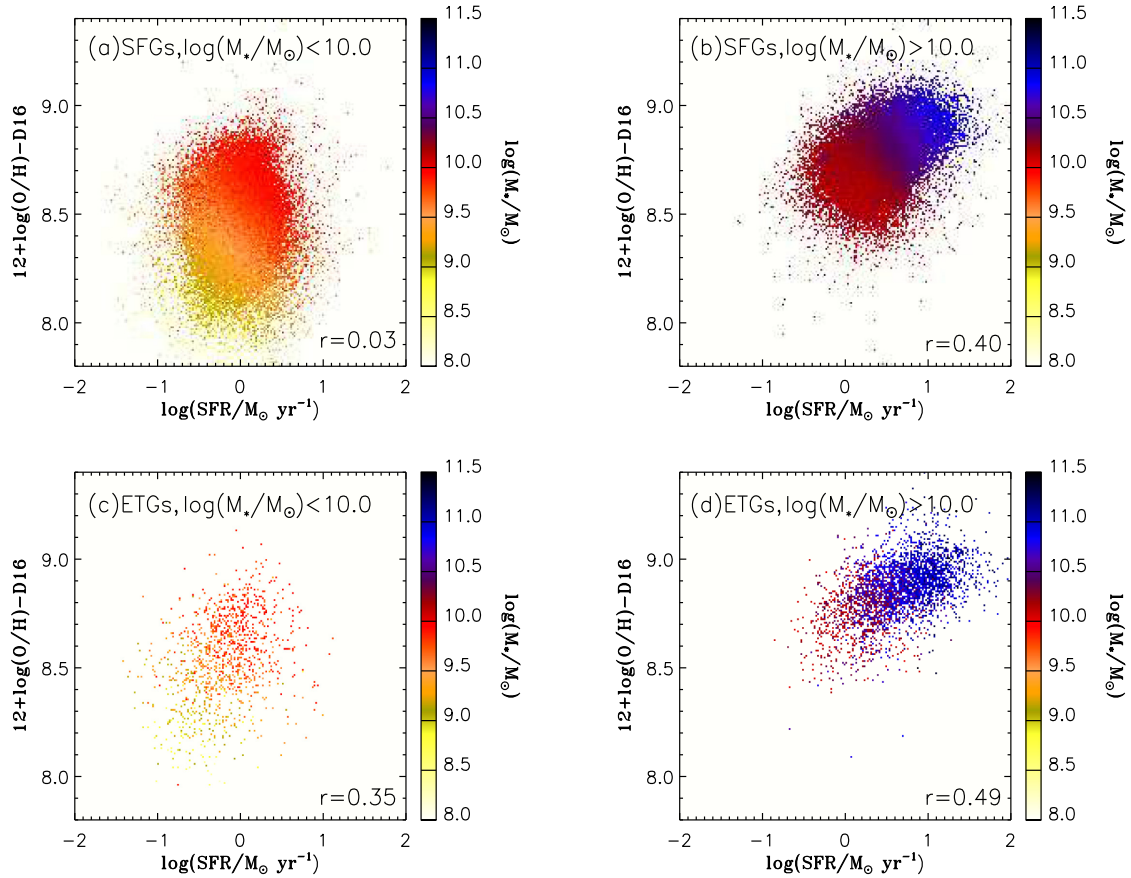
Figure 7. Comparison of SFR–Z relations with the colour bars of stellar mass for star-forming ETGs and SFGs, and these metallicities are calibrated by the D16 indicator.

indicator (the indicator is used simultaneously in this study and Wu et al. 2019). Figs 7(a) and (b) describe the SFR–Z relations for SFGs (35 845 and 47 314 galaxies, respectively) at $\log(M_*/M_\odot) < 10.0$ and $\log(M_*/M_\odot) > 10.0$, respectively, and their Spearman coefficients are $r = 0.03$ and $r = 0.40$. In the sample of 83 159 SFGs, the SFR–Z relation shows a Spearman coefficient $r = 0.50$. In Figs 7(c) and (d), we display the SFR–Z distributions for star-forming ETGs (1188 and 3427 ETGs, respectively) at $\log(M_*/M_\odot) < 10.0$ and $\log(M_*/M_\odot) > 10.0$, respectively (with their Spearman coefficients of $r = 0.35$ and $r = 0.49$). In fact, these correlation coefficients that we have utilized are valid only when the two variables have a monotonic relationship. In Figs 7(a) and (b), we can see that the metallicity increases with decreasing SFR at a fixed stellar mass, $\log(M_*/M_\odot \lesssim 10.5$. In Figs 7(c) and (d), we also seem to find the result at a given stellar mass. This is consistent with that found in fig. 1 of Mannucci et al. (2010), where galaxies with $\log(M_*/M_\odot) < 10.9$ present a negative correlation. From Figs 7(a)–(d), we find that the SFR–Z relation of star-forming ETGs has a stronger correlation than that of SFGs. Although the two types of galaxies have different sample sizes, in general star-forming ETGs present a better correlation for the SFR–Z relation than SFGs.

Wu (2021) found that the weak correlation between SFR and $12 + \log(O/H)$ may originate from metallicity dilution induced by minor mergers. From fig. 7 of Wu (2021), we can see that composite ETGs with lower stellar mass tend to present lower SFRs. Thus, they often have a small amount of ISM compared with massive ETGs, while minor mergers with gas-rich dwarfs

can provide the gas, accreted into the centre of the galaxy. It is easier for the inflow of metal-poor gas induced by minor mergers to dilute the metallicity of these ETGs than that of massive ETGs (Wu 2021). In SFGs, there are the three primary relations that involve the stellar mass, SFR and metallicity. Generally, the strongest correlation is the M–SFR relation, an almost linear relation between the logarithm of both quantities. Then, the tighter correlation is the MZ relation, and finally the SFR–Z relation. The SFR–Z relation is, in general, considered to be a consequence of the other two relations.

In this study, we show the three relations for star-forming ETGs in Figs 4–6, respectively. Fig. 4 presents the strongest correlation for star-forming ETGs, with the Spearman coefficient $r = 0.82$. The stronger correlation appears in the MZ relations of Fig. 5, compared with the SFR–Z relation of Fig. 6. We can see that the correlations of these primary relations decrease with the order of M–SFR, MZ and SFR–Z. This shows that star-forming ETGs also conform to the same sequence of the three primary relations for SFGs. In addition to the global properties of star-forming ETGs, Fig. 7 compares the SFR–Z relations with the colour bar of stellar mass at $\log(M_*/M_\odot) < 10.0$ and $\log(M_*/M_\odot) > 10.0$ for the two types of galaxies. Star-forming ETGs are basically consistent with the various properties of SFGs. Based on the discussion mentioned above, we suggest that the correlation of the SFR–Z relation can be attributed as a consequence of the other two relations.

The question is whether our results could be affected by the metallicity gradient. Although some galaxies show an apparent

flattening or drop of the metallicity in the central or outer regions, the well-known negative abundance gradient has been confirmed by different observations (Zaritsky, Kennicutt & Huchra 1994; Sánchez et al. 2012, 2014; Esteban & García-Rojas 2018; Sánchez 2020). In our study, the overestimation of oxygen abundances induced by the negative gradient may result in some insignificant changes of the corrections and scatters for the MZ and SFR–Z relations. This should not change the main trends of our results due to the entire and small corrections for ETGs.

In addition, from the *GALEX* results we find that the low-level star formation in ETGs preferentially occurs at the outskirts of a galaxy (Fang et al. 2012; Salim et al. 2012). As star formation occurs mostly at the ETG outskirts (Gomes et al. 2016), the total SFRs of these ETGs may be underestimated. Because of low-efficiency star formation, our main results cannot be changed by the SFRs that are underestimated, although these ETGs may have star formation at the outskirts. In ETGs, the inflow material fuelling low-level star formation may result in their metallicity decreasing (Davis & Young 2019), while the metallicities calibrated for the 3-arcsec aperture might be overestimated. However, these overestimating metallicities do not influence our results in a statistically significant way.

5 SUMMARY

In this work, we have collected observational data for 4615 star-forming ETGs, derived by cross-matching the Galaxy Zoo 1 and SDSS DR7 MPA–JHU emission-line measurements. We show the properties of various parameters in the star-forming ETG sample, and we investigate their metallicities with six abundance indicators. Our main results are summarized as follows.

(i) In our star-forming ETG sample, the distribution of stellar mass has a wider range. The median stellar mass of our sample is lower by ~ 0.25 dex than that of composite ETGs. Moreover, the SFR distribution is concentrated at $-0.7 < \log(\mathrm{SFR}/(\mathrm{M_\odot\,yr^{-1}})) < 1.2$, and the median value of SFRs of our sample is slightly higher than that shown in Davis & Young (2019).

(ii) We show a clear trend that lower/higher stellar mass ETGs have lower/higher SFRs. We derive the best fit of $\log(\mathrm{SFR}/(\mathrm{M_\odot\,yr^{-1}})) = (0.74 \pm -.01)\log(\mathrm{M_*/M_\odot}) - (7.22 \pm 0.08)$ for our ETG sample, and our data have the same slope as that found in Cano-Díaz et al. (2019). This shows that our star-forming ETGs locate on the main sequence of SFGs.

(iii) The MZ relations of star-forming ETGs are shown with six abundance indicators. Compared with composite ETGs, most MZ relations present significantly a positive correlation in our ETGs. We find higher metallicity measurements calibrated by the D16, Sanch18 and Sander18 indicators in star-forming ETGs. We suggest that the higher metallicity measurements for star-forming ETGs can be attributed to larger [N II]/Hα ratios induced by the DIG contamination, although these ETGs are mainly ionized by star formation.

(iv) Star-forming ETGs with low-level star formation are similar to the general population of SFGs, and their ionization may be dominated by star formation, but they present a mix of other ionization sources, as they are at least partially retired.

(v) The SFR–Z relations are displayed using six abundance indicators, showing clearly a positive correlation in five indicators. The correlation conforms with the negative correlation between the two parameters in SFGs. The correlation in ETGs may be a consequence of the M–SFR and MZ relations.

DATA AVAILABILITY

The data used in this work are publicly available to access and download as follows:

(i) the catalogue of the MPA–JHU for the SDSS DR7 is available at https://wwwmpa.mpa-garching.mpg.de/SDSS/DR7/;

(ii) the NYU–VAGC for the SDSS DR7 is available at http://sdss.physics.nyu.edu/vagc-dr7/vagc2/sersic/;

(iii) Galaxy Zoo 1 is available at https://data.galaxyzoo.org.

REFERENCES

Abazajian K. N. et al., 2009, ApJS, 182, 543
Alloin D., Collin-Souffrin S., Joly M., Vigrous L., 1979, A&A, 78, 200
Baldry I. K., Glazebrook K., Brinkmann J., Ivezić Ž., Lupton R. H., Nichol R. C., Szalay A. S., 2004, ApJ, 600, 681
Baldwin J. A., Phillips M. M., Terlevich R., 1981, PASP, 93, 5
Belfiore F. et al., 2017, MNRAS, 466, 2570
Bell E. F. et al., 2004, ApJ, 608, 752
Blanton M. R. et al., 2005, AJ, 129, 2562
Brinchmann J., Charlot S., White S. D. M., Tremonti C., Kauffmann G., Heckman T., Brinkmann J., 2004, MNRAS, 351, 1151
Brown M. J. J., Dey A., Jannuzi B. T., Brand K., Benson A. J., Brodwin M., Croton D. J., Eisenhardt P. R., 2007, ApJ, 654, 858
Bryant J. J. et al., 2019, MNRAS, 483, 458
Cano-Díaz M., Ávila-Reese V., Sánchez S. F., Hernández-Toledo H. M., Rodríguez-Puebla A., Boquien M., Ibarra-Medel H., 2019, MNRAS, 488, 3929
Chabrier G., 2003, PASP, 115, 763
Cheung E. et al., 2016, Nature, 533, 504
Chung A., Bureau M., van Gorkom J. H., Koribalski B., 2012, MNRAS, 422, 1083
Cid Fernandes R., Stasińska G., Schlickmann M. S., Mateus A., Vale Asari N., Schoenell W., Sodré L., 2010, MNRAS, 403, 1036
Cortese L., Hughes T. M., 2009, MNRAS, 400, 1225
Crockett R. M. et al., 2011, ApJ, 727, 115
Curti M., Cresci G., Mannucci F., Marconi A., Maiolino R., Esposito S., 2017, MNRAS, 465, 1384
D'Agostino J. J., Kewlwy L. J., Groves B. A., Medling A., Dopita M. A., Thomas A. D., 2019, MNRAS, 485, L38
Davies R. L. et al., 2016, MNRAS, 462, 1616
Davis T. A., Young L. M., 2019, MNRAS, 489, L108
Dopita M. A., Kewley L. J., Sutherland R. S., Nicholls D. C., 2016, AP&SS, 361, 61
Dutton A. A. et al., 2011, MNRAS, 416, 322
Espinosa-Ponce C., Sánchez S. F., Morisset C., Barrera-Ballesteros J. K., Galbany L., García-Benito R., Lacerda E. A. D., Mast D., 2020, MNRAS, 494, 1622
Esteban C., García-Rojas J., 2018, MNRAS, 478, 2315
Faber S. M. et al., 2007, ApJ, 665, 265
Fang J. J., Faber S. M., Salim S., Graves G. J., Rich R. M., 2012, ApJ, 761, 23
Gomes J. M. et al., 2016, A&A, 585, A92
Herpich F., Stasińska G., Mateus A., Vale Asari N., Cid Fernandes R., 2018, MNRAS, 481, 1774
Iglesias-Páramo J. et al., 2016, ApJ, 826, 71
Jones T., Martin C., Cooper M. C., 2015, ApJ, 813, 126
Kauffmann G. et al., 2003a, MNRAS, 346, 1055
Kauffmann G. et al., 2003b, MNRAS, 341, 33

Kaviraj S. et al., 2007, ApJS, 173, 619

Kewley L. J., Dopita M. A., Sutherland R. S., Heisler C. A., Trevena J., 2001, ApJ, 556, 121

Kewley L. J., Jansen R. A., Geller M. J., 2005, PASP, 117, 227

Kroupa P., 2001, MNRAS, 322, 231

Lacerda E. A. D. et al., 2018, MNRAS, 474, 3727

Lacerda E. A. D., Sánchez S. F., Cid Fernandes R., López-Cobá C., Espinosa-Ponce C., Galbany L., 2020, MNRAS, 492, 3073

Lagos C. d. P., Davis T. A., Lacey C. G., Zwaan M. A., Baugh C. M., Gonzalez-Perez V., Padilla N. D., 2014, MNRAS, 443, 1002

Lian J. H., Li J. R., Yan W., Kong X., 2015, MNRAS, 446, 1449

Lintott C. J. et al., 2008, MNRAS, 389, 1179

Lintott C. J. et al., 2011, MNRAS, 410, 166

López-Cabá C. et al., 2020, AJ, 159, 167

Mannucci F., Cresci G., Maiolino R., Marconi A., Gnerucci A., 2010, MNRAS, 408, 2115

Marino R. A. et al., 2013, A&A, 559, A114

Mast D. et al., 2014, A&A, 561, A129

Nagao T., Maiolino R., Marconi A., 2006, A&A, 459, 85

Noeske K. G. et al., 2007, ApJ, 660, L43

Panter B., Jimenez R., Heavens A. F., Charlot S., 2007, MNRAS, 378, 1550

Pettini M., Pagel B. E. J., 2004, MNRAS, 348, 59

Pérez-Montero E., Contini T., 2009, MNRAS, 398, 949

Salim S., Fang J. J., Rich R. M., Raber S. M., Thilker D. A., 2012, ApJ, 755, 105

Salpeter E. E., 1955, ApJ, 121, 161

Sanders R. L. et al., 2018, ApJ, 858, 99

Schawinski K. et al., 2009, MNRAS, 396, 818

Singh R. et al., 2013, A&A, 558, A43

Stasińska G. et al., 2008, MNRAS, 391, L29

Sánchez S. F., 2020, ARA&A, 58, 99

Sánchez S. F. et al., 2012, A&A, 538, A8

Sánchez S. F. et al., 2014, A&A, 563, A49

Sánchez S. F., Walcher C. J., López-Cabá C., Barrera-Ballesteros J. K., Mejia-Narvaez A., Espinosa-Ponce C., Camps-Fariña A., 2020, preprint (arXiv:2009.00424)

Sánchez-Almeida J., Morales-Luis A. B., Muñoz-Tuñón C., Elmegreen D. M., Elmegreen B. G., Méndez-Abreu J., 2018, MNRAS, 476, 4765

Wu Y-Z., 2020, ApJ, 893, L33

Wu Y-Z., 2021, ApJS, 252, 8

Wu Y-Z., Zhang S-N., 2013, MNRAS, 436, 934

Wu Y-Z., Zhang W., Zhao Y-H., 2019, MNRAS, 486, 5310

Yates R. M., Kauffmann G., 2014, MNRAS, 439, 3817

Yi S. K. et al., 2005, ApJ, 619, L111

Young L. M., 2005, ApJ, 634, 258

Zaritsky D., Kennicutt R. C., Huchra J. P., 1994, ApJ, 420, 87

Zhang K. et al., 2017, MNRAS, 466, 3217

This paper has been typeset from a TEX/LATEX file prepared by the author.